

Topographic and Geomorphological Mapping and Analysis of the Chang'E-4 Landing Site on the Far Side of the Moon

Bo Wu, Fei Li, Han Hu, Yang Zhao, Yiran Wang, Peipei Xiao, Yuan Li, Wai Chung Liu, Long Chen, Xuming Ge, Mei Yang, Yingqiao Xu, Qing Ye, Xueying Wu, and He Zhang

Abstract

The Chinese lunar probe Chang'E-4 successfully landed in the Von Kármán crater on the far side of the Moon. This paper presents the topographic and geomorphological mapping and their joint analysis for selecting the Chang'E-4 landing site in the Von Kármán crater. A digital topographic model (DTM) of the Von Kármán crater, with a spatial resolution of 30 m, was generated through the integrated processing of Chang'E-2 images (7 m/pixel) and Lunar Reconnaissance Orbiter (LRO) Laser Altimeter (LOLA) data. Slope maps were derived from the DTM. Terrain occlusions to both the Sun and the relay satellite were studied. Craters with diameters ≥ 70 m were detected to generate a crater density map. Rocks with diameters ≥ 2 m were also extracted to generate a rock abundance map using an LRO narrow angle camera (NAC) image mosaic. The joint topographic and geomorphological analysis identified three subregions for landing. One of them, recommended as the highest-priority landing site, was the one in which Chang'E-4 eventually landed. After the successful landing of Chang'E-4, we immediately determined the precise location of the lander by the integrated processing of orbiter, descent and ground images. We also conducted a detailed analysis around the landing location. The results revealed that the Chang'E-4

lander has excellent visibility to the Sun and relay satellite; the lander is on a slope of about 4.5° towards the southwest, and the rock abundance around the landing location is almost 0. The developed methods and results can benefit future soft-landing missions to the Moon and other celestial bodies.

Introduction

On 3 January 2019, the Chinese lunar probe Chang'E-4, carrying the Jade Rabbit-2 lunar rover, successfully landed in the Von Kármán crater in the northwestern South Pole-Aitken (SPA) basin on the far side of the Moon (Figure 1). Chang'E-4 was the first spacecraft to make a soft landing on the lunar far side. The Chang'E-4 lander and the Jade Rabbit-2 rover are now exploring the surface and subsurface of the Von Kármán crater's mare-covered floor with their onboard scientific instruments. Their tasks include investigating the compositions of mare basalt and the subsurface structure of the regolith of this far side region (Wu *et al.* 2017), and finding clues that could provide insight into the early geologic history of the Moon (Wilhelms, John, and Trask 1987; Huang *et al.* 2018; Li *et al.* 2019; Di *et al.* 2019).

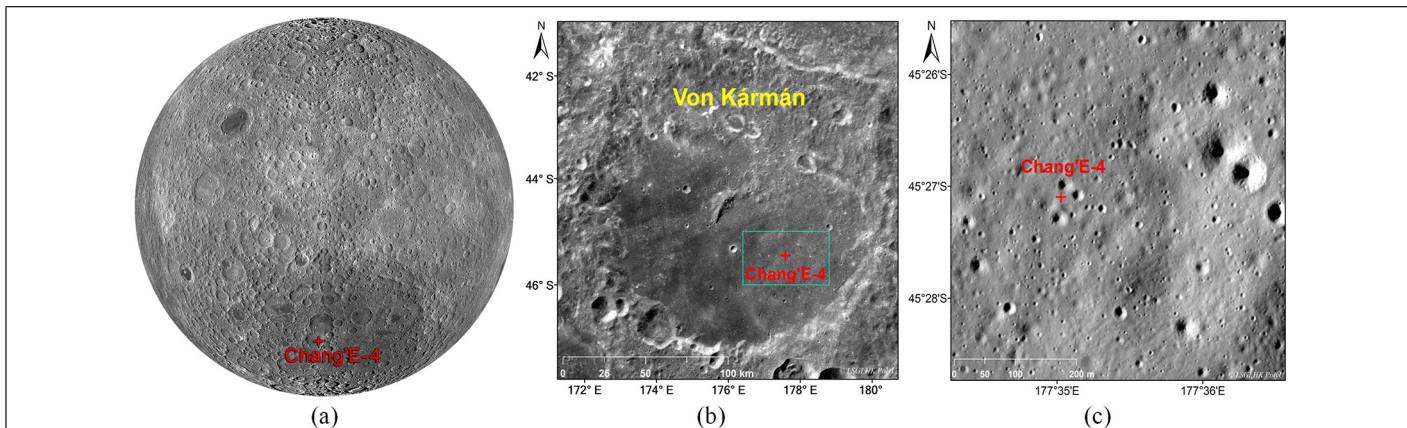


Figure 1. The Chang'E-4 landing site. (a) The landing site shown in a global view of the far side of the Moon; (b) an enlarged view of the landing site inside the Von Kármán crater shown in a Chang'E-2 image, with the green box indicating the targeted landing region; and (c) a further enlarged view of the landing site shown in a LRO NAC image.

Bo Wu, Han Hu, Yiran Wang, Peipei Xiao, Yuan Li, Wai Chung Liu, Long Chen, and Xuming Ge are with the Department of Land Surveying and Geo-Informatics, The Hong Kong Polytechnic University, Hung Hom, Kowloon, Hong Kong (bo.wu@polyu.edu.hk).

Fei Li, Yang Zhao, Mei Yang, Yingqiao Xu, Qing Ye, Xueying Wu, and He Zhang are with the China Academy of Space Technology, 104 Youyi Street, Haidian, Beijing, P.R. China (kuokulee@163.com).

Photogrammetric Engineering & Remote Sensing
Vol. 86, No. 4, April 2020, pp. 247–258.
0099-1112/20/247-258

© 2020 American Society for Photogrammetry
and Remote Sensing
doi: 10.14358/PERS.86.4.247

Chang'E-4 is part of the second phase of the Chinese Lunar Exploration Program (Wu *et al.* 2017; Jia *et al.* 2018). This probe is a former backup of the Chang'E-3 probe (Jia *et al.* 2018), which made a successful lunar landing in the Sinus Iridum region in the Mare Imbrium on 14 December 2013 (Wu *et al.* 2014a). Unlike the landing site of the Chang'E-3, the targeted landing region of Chang'E-4 is on the far side of the Moon; therefore, a relay satellite was sent to the Earth-Moon Lagrangian Point 2 (L2) halo orbit in May 2018, which serves as a communication relay station between Earth and the lunar far side (Jia *et al.* 2018).

The selection of the Chang'E-4 landing site includes several steps. In the first step, two craters located inside the SPA basin, including the Von Kármán crater and the nearby Chretien crater, were selected. This is because a similar latitude to the Chang'E-3 landing site was preferred (i.e., at about 45°S in latitude) and due to the temperature and communication constraints. At the latitude of about 45°S inside the SPA basin, the Von Kármán crater and Chretien crater are superior to others in terms of crater size and roughness of the crater floor. In the second step, two candidate landing regions located inside the Von Kármán crater and Chretien crater, each covering an area of about 50 × 30 square kilometers, were selected for detailed analysis in terms of surface elevations, terrain slopes, and terrain occlusions to sun illumination and telecommunication. The candidate landing region located in the southeast floor of the Von Kármán crater, outlined in Figure 1b by the green box, was chosen based on its superiority in all these aspects.

To ensure a safe and successful landing, a careful analysis of the topography and geomorphology (De Rosa *et al.* 2012; Wu *et al.* 2014a) of the targeted landing region for further selecting a suitable landing site is critical. Topographic features, such as surface slopes and occlusions, along with geomorphological features such as the distributions of craters and boulders/rocks, were mapped and analyzed to identify the best suitable site for landing. In this research, we created digital topographic models (DTMs) of the Von Kármán crater at a spatial resolution of 30 m through the integrated processing of Chang'E-2 images and Lunar Reconnaissance Orbiter (LRO) Laser Altimeter (LOLA) data (Wu, Hu, Guo 2014b). Based on the DTMs, we scrutinized the surface slopes and terrain occlusions to the solar illumination and the relay satellite. Based on the Chang'E-2 images and the high-resolution LRO narrow angle camera (NAC) images, we analyzed the crater distribution and rock abundance inside the targeted landing region. The topographic and geomorphological features were then analyzed jointly to identify three subregions for landing. Chang'E-4 eventually landed in the subregion of the highest priority on 3 January 2019. After the landing, we precisely located the lander by using the images collected both in orbit and during the descent phase, together with a ground panorama collected by the lander's overhead camera upon landing. A detailed terrain occlusion analysis around the landing location was performed, and a 1.5 m/pixel DTM was generated using the shape-from-shading (SFS) approach (Wu *et al.* 2018a). This made it possible to conduct detailed topographic analyses to support the surface operations of the lander and rover.

This paper focuses on the targeted landing region inside the Von Kármán crater. It is organized as follows. The next section describes the methods and results regarding topographic mapping, with the topic of geomorphological mapping reserved for the section "Geomorphologic Mapping and Analysis of the Landing Region". The joint topographic and geomorphological analysis with the purpose of identifying subregions for landing are presented in the subsequent section. The section "Landing Site Localization and Analysis" includes further results regarding the precision localization of the lander and a detailed analysis of the surface slopes and occlusions around the landing site. Finally, the last section offers concluding remarks and discussion.

Topographic Mapping and Analysis of the Landing Region

Topographic Mapping

High-resolution DTMs are the vital data resources for topographic analysis of the targeted landing region. Currently, the Selenological and Engineering Explorer (SELENE) and LRO digital elevation model (SLDEM) generated by the co-registration of the photogrammetric results from the SELENE imagery and the LOLA measurements (Barker *et al.* 2016), provides full coverage of the targeted landing region at a spatial resolution of about 60 m. The SLDEM offers a typical vertical accuracy of 3 to 4 m. The SLDEM has favorable geometric accuracies but sparse spatial resolution. In this research, we used the Chang'E-2 images (7 m/pixel) covering the Von Kármán crater to generate a DTM with a spatial resolution of 30 m by the integrated processing with the LOLA measurements (Wu, Hu, Guo 2014b).

The Chang'E-2 camera consists of two linear push broom sensors with a convergence angle of about 25° that are used to formulate an along-track stereo configuration of the images (Wu, Hu, Guo 2014b). There is an overlap of about 50% between the images in the adjacent tracks. We developed a combined block adjustment approach for the integrated processing of the multiple-track Chang'E-2 images and the LOLA measurements to generate high-precision DTMs. By doing so, inconsistencies can be reduced between the multiple-track Chang'E-2 images, and between the three-dimensional (3D) measurements from the Chang'E-2 images and the LOLA measurements. This approach was used for the integrated processing of the Chang'E-2 images and LOLA measurements covering the Von Kármán crater and thus improved the orientation parameters of Chang'E-2 images. Dense image matching was carried out on the stereo Chang'E-2 images to generate dense matches, using a texture-aware semiglobal matching algorithm (Hu *et al.* 2016). 3D point clouds were then generated from the matching results based on the improved image orientation parameters, and finally, a DTM of the region with a spatial resolution of 30 m was interpolated from the 3D point clouds. The generated DTM was compared with the SLDEM covering the same region. The results indicated that the former has a degree of geometric accuracy similar to the latter but offers better spatial resolution (Hu and Wu 2019).

Figure 2a shows a 3D view of the generated DTM covering the Von Kármán crater. The right column shows an enlarged view of the targeted landing region as marked with a red box in the left column. Based on the generated DTM, the Von Kármán crater measures about 180 km in diameter, with a rim-to-floor depth of about 5 km. The crater floor has a diameter of about 140 km, and there is a central peak of about 1.55 km in height in the middle part of the crater. Within the targeted landing region, the terrain surface has a minimum height of -6076 m and a maximum height of -5776 m, respectively, with respect to a reference sphere of radius 1737.4 km. Figure 2b shows the generated ortho-image mosaics. Based on the generated DTM, the Chang'E-2 images were ortho-rectified and mosaicked to generate an orthographic image mosaic covering the Von Kármán crater, as shown in the left column of Figure 2b, which has the same resolution of 7 m/pixel as the original Chang'E-2 images. Inside the targeted landing region, LRO NAC images were collected to generate an image mosaic with a higher spatial resolution (1.5 m/pixel), as shown in the right column of Figure 2b.

Slope Analysis

Surface slope is an important engineering constraint in landing site evaluation to ensure the stability of the lander during touchdown, which is the magnitude of the derivatives of the gridded topographic model (i.e., the DTM) at a specific baseline. With two grid cells required for slope calculation along one direction, the corresponding baseline for slope analysis is two times the spatial resolution of the DTM, which is 60

m for the DTM generated from the Chang'E-2 images. For any point in the DTM, slopes along the east-west and north-south directions are calculated based on the distance and elevation difference of the two neighboring grid cells, and the square root of the sum of their squares is calculated as the maximum slope at that point. The slope calculation method is consistent with those provided in popular software systems, such as ArcGIS. After the slopes of all the points in the DTM have been calculated, a slope map can be generated. Figure 3 shows the slope map and statistics of the targeted landing region at a baseline of 60 m. It can be seen that most of the region (99.7%) has slopes of less than 15°, and 96.9% of the region has slopes of less than 8°. Only 3.1% of the region has slopes larger than 8°, and those areas are mainly distributed inside some craters.

A baseline of 8 m is further imposed for slope analysis, considering the lander footprint size of about 4.5 m plus a buffer for attitude adjustment of the lander before touchdown. However, slope analysis at an 8-m baseline requires a higher resolution DTM. There is only one stereo pair of LRO NAC images covering a small portion of the middle-north part of the landing region that could be used to generate a DTM of 4 m resolution. No high-resolution DTMs are available for other areas inside the landing region. In our previous work (Wang and Wu 2017), we presented a correlation analysis of slopes derived from the same terrain surface with different baselines. The results indicated that it is possible to estimate slopes at short baselines from slopes calculated from relatively longer baselines. The same method was used here for the estimation of slopes at different baselines. The 4-m resolution DTM from the stereo NAC images and the corresponding 30-m resolution DTM from the Chang'E-2 images, both covering the same local area inside the landing region, were used for correlation analysis of slopes at baselines of 8 m and 60 m. A slope amplification function with multipliers in the range of [1.1, 1.6] was obtained from the correlation analysis in this local area, which was then used for estimation of slopes at 8-m baseline in other areas inside the landing region, based on the assumption that the influences of different baselines on slopes should be similar for this local area and its nearby region. Therefore, we also compute an aggressive (the lower amplification bound of 1.1) and a conservative (the upper amplification bound of 1.6) estimation of the slopes at the 8 m baseline based on the original slopes at 60 m baseline. In the case of conservative estimations, about 3.4% of the areas have slopes larger than 8°, and this value only rises to about 5%, even in the aggressive case. Similarly, the areas with larger slopes are located inside the craters.

Occlusion Analysis

As the targeted landing region is on the floor of the Von Kármán crater and the height difference from the floor to the crater rim is about 5 km, it is crucial to analyze the possible terrain occlusions to solar illumination and communication signals from the relay satellite. The lander and rover rely on solar energy to charge the batteries of the onboard instruments. Also, communications and data transfer between the Earth control center and the lander require that the latter stays

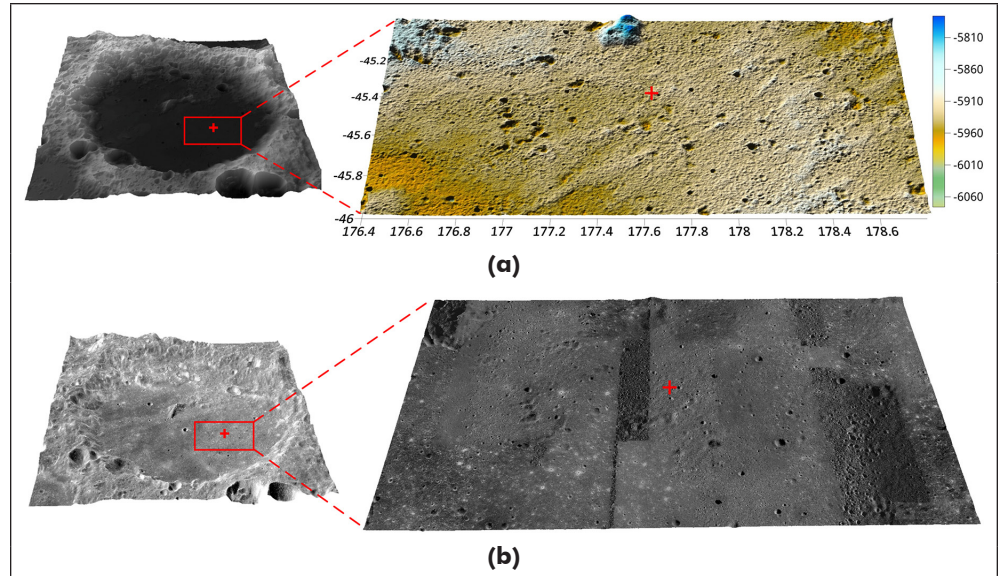


Figure 2. Topographic mapping results of the Von Kármán crater. (a) 3D view of the DTM (30 m/pixel), (b) 3D view of the orthographic image mosaics projected on the DTM. The left column shows the Chang'E-2 image mosaic (7 m/pixel), and the right column shows the LRO NAC image mosaic (1.5 m/pixel) in the targeted landing region. The red cross indicates the landing location.

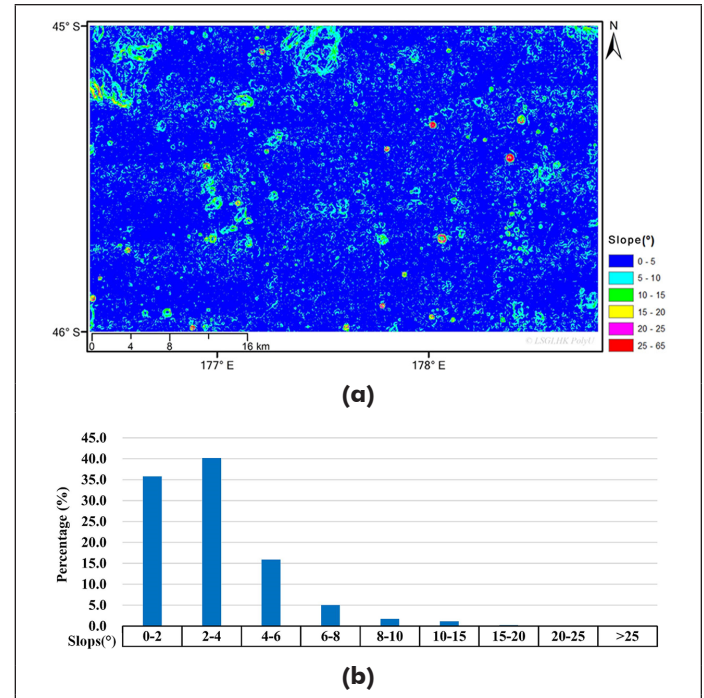


Figure 3. Slope map and statistics of the targeted landing region. (a) The slope map at a baseline of 60 m and (b) histogram of the slope statistics.

in the sight of the relay satellite. Therefore, areas with maximum visibility of the Sun and the relay satellite, that is, areas that feature the least amount of occlusion from the terrain, are preferred when evaluating landing site suitability.

In the analysis of the occlusion conditions caused by the terrain, a search radius of 200 km surrounding the targeted landing region is considered, to enclose the entire rim of the Von Kármán crater and some high mountains outside the crater that may cause occlusions. Due to the long distances involved when calculating terrain occlusion angles, the curvature of the lunar surface cannot be ignored. An approach

based on the geodesic line (Karney 2013) was developed to analyze the altitude angles of terrain occlusions, as illustrated in Figure 4. For each target point $A(\lambda_1, \varphi_1)$ at longitude λ_1 and latitude φ_1 in the landing region, a geodesic line l is determined by a specific azimuth angle α . Given a specific distance s_{12} , the geographic coordinates of the search point $B(\lambda_2, \varphi_2)$ can be determined based on the geodesic line (Karney 2013). The height of point B can be sampled from the DTM. Then, the 3D coordinates of B can be projected to a local Cartesian coordinate system of the target point A , in which the altitude and distance of B , with respect to the target point A , can be determined, and an altitude angle θ can be calculated to represent the terrain occlusion of point B to A . The process just described is repeated for all of the azimuth angles and the entire search radius of 200 km. The intervals for the azimuth angle α and geodesic distance s_{12} are set to be 1° and the spatial resolution of the DTM, respectively, considering the accuracy in capturing the topographic features and the processing time. Next, the maximum occlusion angle for point A along each azimuth direction can be determined, and the maximum occlusion angle among all the azimuth directions from 0° to 360° can be obtained. This procedure is further repeated for each grid point in the targeted landing region to generate the terrain occlusion map shown in Figure 5.

Figure 5 shows the terrain occlusion maps of the targeted landing region. Figure 5a shows the maximum altitude angle of terrain occlusion for each point inside the region, and Figure 5b shows the corresponding azimuth of the maximum altitude angle for each point. For most of the flat areas inside the landing region, the maximum terrain altitude angle is less than 10° . Also, most of the maximum altitude angles are caused by the rims of the Von Kármán crater in the southeast and east parts, as indicated by the azimuth map of terrain occlusion in Figure 5b. In the targeted landing region located in the southeast part of the crater floor, as shown in Figure 1, the southeast and east parts of the crater rim create larger terrain occlusions because they are closer to the landing region. In contrast, terrain occlusions in the northwest corner of Figure 5b show that the terrain occlusions in this part come from the northwest direction, either from the rim of the Von Kármán crater far to the northwest at a far distance or from the nearby central peak of Von Kármán crater, also located in the northwest of the landing region. The large terrain occlusions indicated in red or yellow in Figure 5a are inside the craters and along the slopes of the hills.

For a period of six months after the landing of Chang'E-4, from 3 January to 3 July 2019 (the designed working period of Chang'E-4), the solar azimuth and altitude of each point inside the landing region can be obtained from ephemeris information and compared with the altitude angle of the terrain occlusion along the same azimuth. The solar occlusion conditions are derived for each point by summarizing the possible occlusions of all the solar azimuth directions. Figure 6a presents the resulting percentage of visibility of the Sun during the six-month period over the entire region, with red representing occlusions to the Sun. It should be noted that the lander and rover hibernate during the lunar night and they will automatically wake up when the solar altitude angle is greater than 10° ; therefore, only the time slots with solar altitude angles greater than 10° (43.7% of the designed working period of six months) were considered in the above occlusion analysis. It can be seen from Figure 6a that a majority (99.8%) of the landing region has 100% visibility of the Sun during the six-month period (excluding the time when the solar altitude angles are $\leq 10^\circ$); however, in some areas, especially inside small craters and near hills, the solar visibility is as low as 86%.

Figure 6b presents the terrain occlusions to the relay satellite. As mentioned earlier, a relay satellite was sent to the Earth-Moon L2 point and stayed there in a halo orbit to provide continuous communication between the Earth

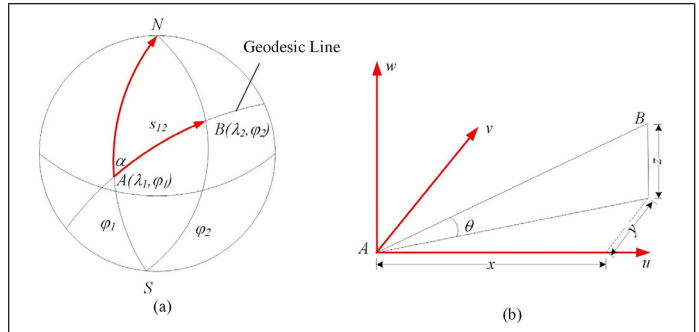


Figure 4. Computation of terrain occlusions based on the geodesic line. (a) The terrain occlusion is searched along the geodesic line for a specific target point A and sampled by a uniform interval. (b) The searched point B is projected to the local Cartesian coordinate system of target point A and the altitude angle of terrain occlusion is calculated.

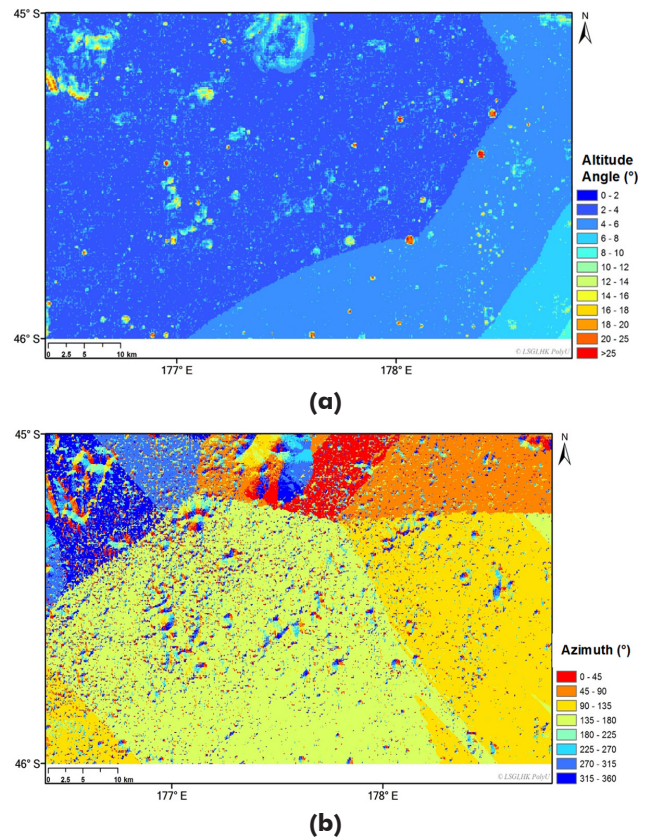
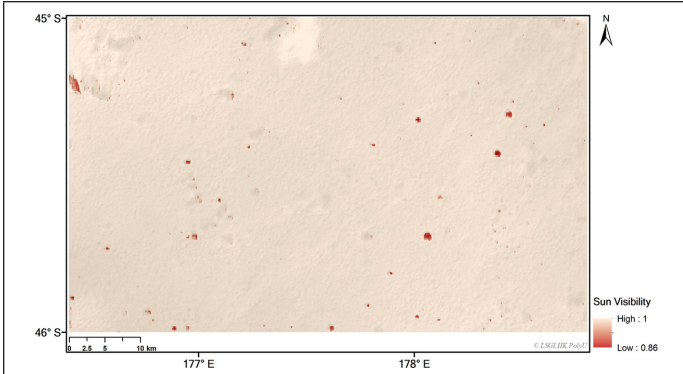
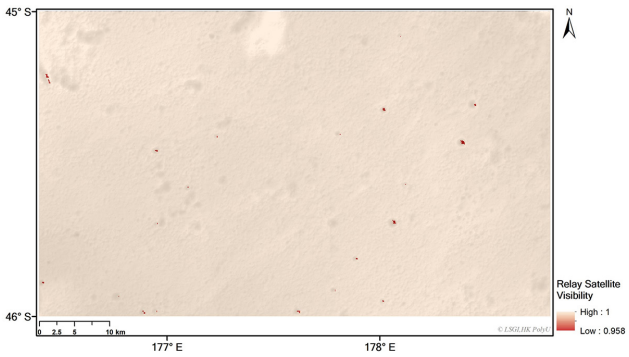


Figure 5. Terrain occlusion maps of the targeted landing region. (a) The maximum altitude angles of terrain occlusion for each point in all azimuth directions, (b) the corresponding azimuth angles for the maximum occlusion of each point.

control center and the Chang'E-4 lander on the far side of the Moon. For the same period of six months after the landing of Chang'E-4, the azimuth and altitude of the relay satellite with respect to each point inside the landing region were estimated from the orbit design of the relay satellite. An occlusion map to the relay satellite for the entire landing region was generated following the same process as for occlusion to the Sun, as shown in Figure 6b. As before, the time slots with solar altitude angles less than 10° , when the lander and rover hibernate, were ignored in the occlusion analysis. From Figure 6b, the relay satellite is 100% visible over the majority (99.98%) of the landing region during the six-month period of interest. Nevertheless, there are several places, shown in red, where the relay



(a)



(b)

Figure 6. Visibility maps of the targeted landing region for the six-month period after the landing of Chang'E-4 from 3 January to 3 July 2019. (a) Visibility map to the Sun and (b) visibility map to the relay satellite.

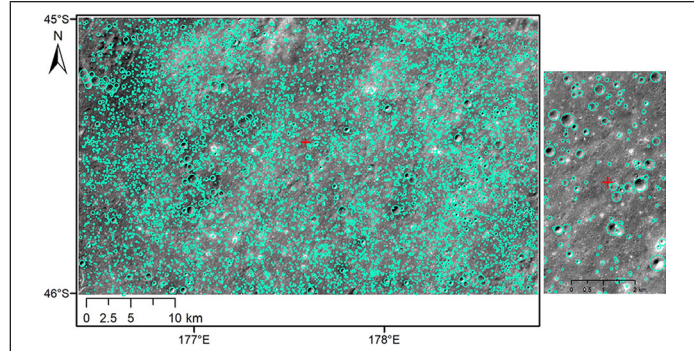
satellite is visible only for 95.8% of the time. Fortunately, these places are rare and are distributed mainly inside a few craters or around the foot of the hill in the northwest of the landing region. The occlusions to the relay satellite are less severe compared with the occlusions to the Sun, as can be noted from Figure 6. This is reasonable considering that the altitudes of the relay satellite, with respect to the targeted landing region, are consistently larger than $\sim 25^\circ$ by the design of the halo orbit.

Geomorphologic Mapping and Analysis of the Landing Region

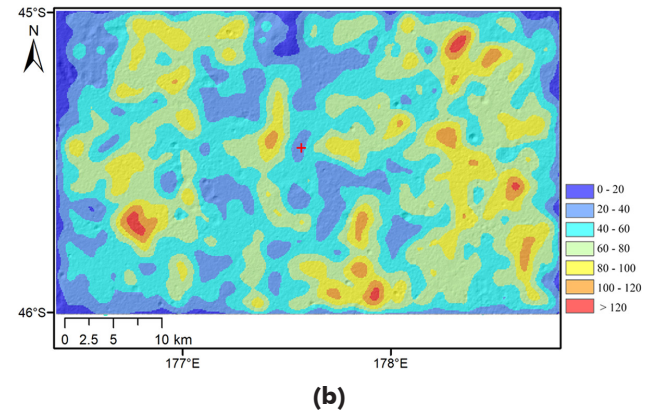
Crater Distribution

Craters are common geomorphologic features on the Moon. Craters are considered possible hazards in landing site evaluation due to their internal slopes and protuberant rims. Therefore, a lower crater density is preferred in selecting the landing site. Also, Chang'E-4 had to avoid landing in any small craters (a few meters to dozens of meters in diameter) to allow the maximum maneuvering capability of the rover (Brady *et al.* 2009; Wu *et al.* 2014a).

We developed an active machine-learning algorithm (Wang and Wu 2019) for automatic crater detection in the targeted landing region. The 7 m/pixel Chang'E-2 image mosaic was used for crater detection inside the landing region. We aimed to identify all craters larger than 70 m in diameter, which is equivalent to 10 pixels on the image, as the performance of our algorithm decreases for craters smaller than 10 pixels in diameter. It should be noted that the LRO NAC image mosaic was not used for crater detection here. Even though it offers higher resolution, LRO NAC imagery has varying illumination conditions and unbalanced image contrasts, as shown in the right column of Figure 2b, which will influence the crater detection and result in biases in crater density analysis across



(a)



(b)

Figure 7. (a) Distribution of craters (≥ 70 m in diameter) in the targeted landing region. The red cross indicates the landing location, and the inset figure on the right shows an enlarged view of the detected craters around the landing location. (b) The crater density map in terms of crater numbers calculated using a moving circular window.

the landing region. By contrast, the Chang'E-2 image mosaic has consistent illumination and contrast conditions, as can be seen in the left column of Figure 2b. After the automatic crater detection on the Chang'E-2 image mosaic using the algorithm (Wang and Wu 2019), a manual checking process was further carried out to ensure the reliability of the detected craters, by digitizing missing craters and removing artifacts with the assistance of a grid with a cell size of $70\text{ m} \times 70\text{ m}$ overlaid on the image mosaic. Ultimately, 9391 craters with diameters ranging from 70 m to 1405 m were detected in the landing region. Figure 7a shows the distribution of those detected craters.

To understand the crater distribution in the targeted landing region, a crater density map depicting crater numbers in a unit area was generated, as shown in Figure 7b. The map was obtained by using a moving circular window with an area of 10 km^2 to count the numbers of craters. Smaller density represents a sparser distribution of craters and thus a relatively safer situation for landing. Figure 7b shows that the eastern part of the targeted landing region has relatively higher crater density compared with the central and western parts. The average crater density in the targeted landing region is about 60 craters over a circular window of 10 km^2 area.

Rock Abundance

Rocks are another type of major feature on the lunar surface that can be hazardous for the lander and rover. Rock abundance, defined as the cumulative fractional area covered by rocks with respect to their diameters, is another crucial factor in evaluating the suitability of finding a landing site for any landing mission (Golombek and Rapp 1997; Golombek *et al.* 2003; De Rosa *et al.* 2012; Wu *et al.* 2018b). For example, one

criterion for selecting the landing site of National Aeronautics and Space Administration's (NASA's) InSight mission on Mars was that the rock abundance had to be less than 10% (Golombek *et al.* 2017); and for the ExoMars mission of the European Space Agency, the rock abundance must be less than 7% (Pajola *et al.* 2017). In this research, a rock abundance constraint of 7% was considered in landing site evaluation given the ability of the lander and rover to tolerate rocks during their maneuvering.

We developed a rock detection algorithm (Li and Wu 2018) to extract rocks from the LRO NAC image mosaic. The algorithm detects rocks based on their particular brightness distributions and relief properties presented in the image. The details pertaining to this rock detection algorithm can be found in our previous work. Using the algorithm, a total of 21 004 rocks were identified from the LRO NAC image mosaic (1.5 m/pixel) covering the targeted landing region. The minimum size of rocks that were detected is 2 m (the longest diameter of the rock boundary), and the maximum size is 17.24 m. The detected rocks were manually checked by two independent operators to further ensure the reliability of rock detection. The distribution of the final detected rocks is shown in Figure 8a.

Figure 8a shows the distribution of rocks larger than 2 m within the targeted landing region. However, for landing site assessment, we will need to understand the overall distribution of rocks of all sizes. A rock abundance model developed by Li and Wu (2018) is used here, which allows us to infer the overall distribution of rocks of all sizes from rocks above a particular size. The rock abundance model has the following exponential format:

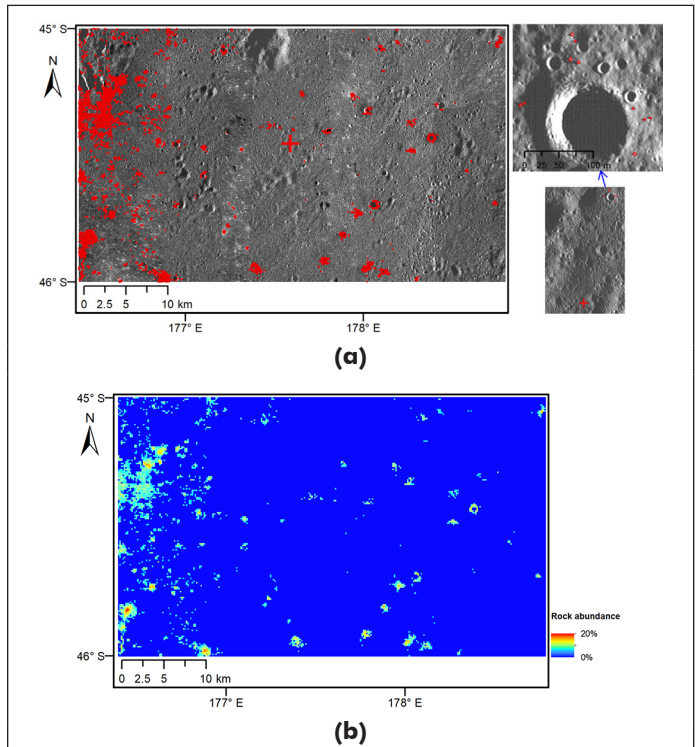


Figure 8. Rock abundances in the targeted landing region. (a) Distribution of rocks larger than 2 m in diameter overlaid on the LRO NAC image mosaic. The red cross indicates the landing location, and the inset figures on the right show enlarged views of the detected rocks. (b) The rock abundance map showing the cumulative fractional area of rocks in the region.

$$F_k(D) = ke^{-\left(0.5648 + \frac{0.01285}{k}\right)D} \quad (1)$$

where D is the rock diameter, k is rock abundance, and $F_k(D)$ is the fractional area covered by rocks with diameters larger than D . Based on the rock detection result, the rock abundances were estimated using the above rock abundance model to generate a rock abundance map of the targeted landing region, as shown in Figure 8b. It should be noted that the rock abundance model can only be used to estimate the overall distribution of rocks in an area from the size-frequency distribution of the detected rocks. If no rock is detected from the image in a local area, this either indicates that the area is indeed rock-free, or there might be smaller rocks, but they are ignored. The latter case requires higher-resolution image data for checking the existence of smaller rocks. Nevertheless, the rock abundance map generated from the method above can still be used to analyze the relative rock abundances of different local areas in the targeted landing region.

The rock abundance map shown in Figure 8b was generated by calculating the fractional area of detected rocks within each tile of 250 m × 250 m inside the landing region and by further extrapolating the rock abundance values for each tile based on Equation 1. The tile size of 250 m was selected considering its statistical significance (Li and Wu 2018) and meaningfulness for comparing with LRO Diviner Radiometer data, as described below. According to the rock abundance map and the rock distribution map, as shown in Figure 8, most rocks are located around rocky impact craters and slopes of hills. Within the targeted landing region, 99.9% of the region has a rock abundance of < 7%, and 97.1% of the region has a rock abundance of < 1%. The highest rock abundance in the region is 18.21%, appearing on the slope of a rocky crater close to the south-western boundary of the target landing region located at (176.4488°E, 45.8222°S).

Our rock abundance map is further compared with the rock concentration map obtained from the LRO Diviner Radiometer data. Based on the contrasting thermal conductivities between rocks and lunar regolith, Bandfield *et al.* (2011) derived a rock concentration map (<http://ode.rsl.wustl.edu/moon/index.aspx>) using the LRO Diviner Radiometer data. The same reference system (Mean Earth/Polar Axis) and the same map projection (Mercator) were used for the Diviner map and the LRO NAC image mosaic, and we found that the two maps matched well in general by referring to the locations and shapes of some big craters commonly visible on them. The Diviner map has a spatial resolution of 128 pixels per degree (~250 m at the equator), and each pixel presents an aerial fraction of rocks with diameters larger than ~1 m. To compare with the Diviner map, the areal fraction of rocks ≥ 1 m was extrapolated from our detected rocks (≥ 2 m in diameter), which were then binned into pixels of the same scale of the Diviner bins, using the rock abundance model as shown in Equation 1. The differences between our results and the Diviner map in the landing region are shown in Figure 9a. The average absolute difference between our map and the Diviner map is 0.25%. The greatest positive difference is 12.8%, and the greatest negative difference is -2.2%, as shown in Figure 9b. The first row in Figure 9b shows the case in which the greatest positive difference appears. The fraction area of rocks (≥ 1 m) derived from our rock detection result is as high as 15.1%, while the Diviner result is only 2.3%, leading to a positive difference of 12.8%. Our higher value is more reasonable than the Diviner result considering that the areal fraction of the detected rocks (≥ 2 m) already reaches 8.2%. The reason for this kind of discrepancy might be that craters with various slopes may show a range of temperatures with the Diviner measurements, which may consequently lead to uncertainties

and errors (Li and Wu 2018; Bandfield *et al.* 2011). The second row in Figure 9b shows the greatest negative difference of -2.2% . This type of discrepancy can be attributed to the unfavorable illumination conditions in which rocks cannot be identified in the dark shadows. Fortunately, such shadowed areas cover less than 1% of the landing region.

Joint Topographic and Geomorphological Analysis for Landing Site Selection

The previously described topographic factors, including surface slopes and occlusions, and the geomorphologic factors, including crater distribution and rock abundance, are critical considerations when selecting suitable landing sites for Chang'E-4 to avoid hazards during touchdown and ensure favorable maneuverability of the robotic rover. Therefore, we carried out a joint topographic and geomorphologic analysis to identify subregions inside the targeted landing region that could be favorable for a safe landing.

The Chang'E-4 lander had an orbital inclination angle ranging from 80° to 100° from the east by orbit design dependent on the launching window. There were various uncertainties in orbit determination which might affect the actual landing (Li *et al.* 2017). In the longitude direction, considering the influence of midcourse orbit correction, near-Moon braking, and other orbit control errors, there were certain errors in the orbital inclination relative to the nominal design, which would be propagated along the longitude direction. In addition, simulation analysis of the powered descent phase also revealed kilometer-scale deviations in the longitude direction caused by the powered descent. In the latitude direction, uncertainties included the prediction error of the start point of the powered

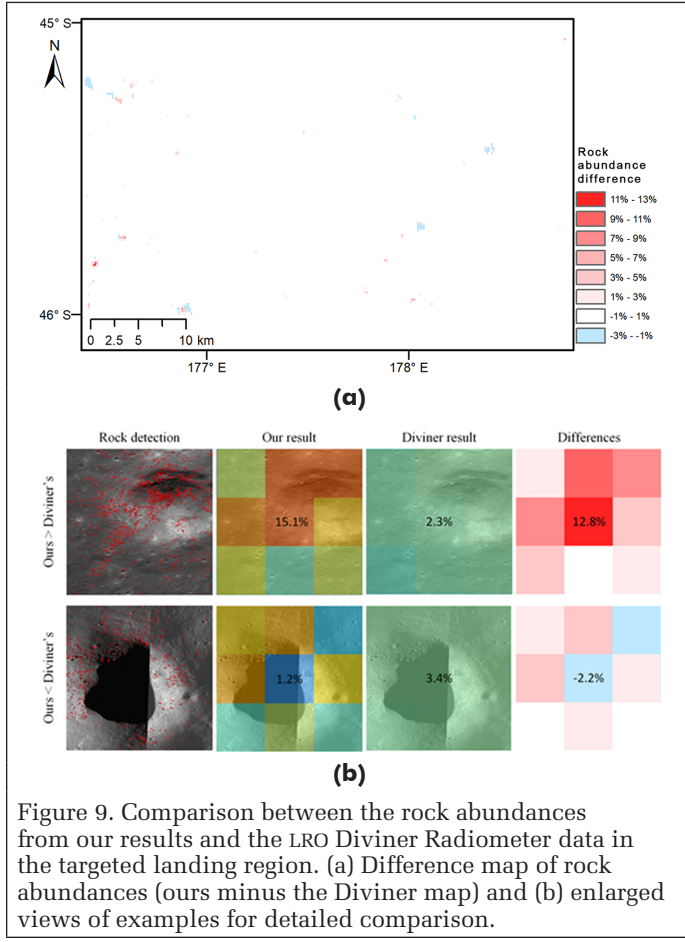


Figure 9. Comparison between the rock abundances from our results and the LRO Diviner Radiometer data in the targeted landing region. (a) Difference map of rock abundances (ours minus the Diviner map) and (b) enlarged views of examples for detailed comparison.

descent phase and the thrust deviation of the 7500 N motor onboard the lander, which were also in kilometer scale. Considering the above engineering factors, a rectangle centered at the orbit track with a width of ± 5 km across the orbit direction and a length of ± 15 km along the orbit direction was defined as a subregion for landing. The targeted landing region was then divided into 25 subregions for detailed analysis, as shown in Figure 10a. There was a 2 km offset between any two neighboring subregions, and the areas beyond the targeted landing region were ignored in the analysis.

For all the 25 subregions, we examined five specific criteria to evaluate their suitability for a safe landing, including surface slopes, terrain occlusions to the Sun, terrain occlusions to the relay satellite, crater densities, and rock abundances. For each criterion, we set a soft threshold and scored the subregion based on the percentage of areas that exceed the threshold. For the slope threshold, 8° was applied on the slopes at the 8 m baseline. For the crater density, the average crater density of the landing region plus its standard deviation was used as the threshold, which was 78 craters (≥ 70 m in diameter) per 10 km^2 . For the rock abundance, 7% was used as the threshold. For the occlusions to both the Sun and relay satellite, we directly counted the percentages of areas with any occlusions during the six-month period after landing with respect to the total area of the subregion. It should be noted that some of these threshold parameters (e.g., slopes and rock abundance) were considered mainly based on the engineering constraints described previously. Some threshold parameters (e.g., the crater density) might not directly relate

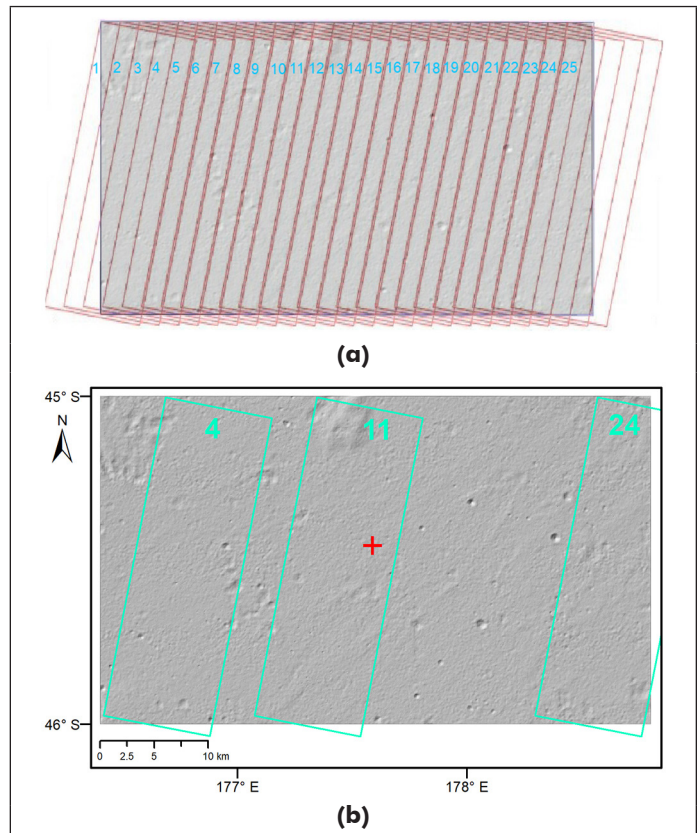


Figure 10. Joint analysis for selecting the subregion for landing. (a) 25 subregions covering the targeted landing region; (b) the three short-listed subregions, with 11 being the highest priority, where Chang'E-4 actually landed. The red cross indicates the exact landing location of Chang'E-4. The underlying image is a shaded relief of the DTM of the targeted landing region.

Table 1. Statistics of slopes, crater densities, rock abundances, and occlusions of the three short-listed subregions.

| Subregion | Slope | | Crater density | | Rock abundance | | Occlusion to the Sun (%) | Occlusion to the relay satellite (%) | Priority as landing site |
|-----------|-------------|---------------------------|----------------------------------------------|----------------------------------------------------|----------------|-----------------------|--------------------------|--------------------------------------|--------------------------|
| | Average (°) | % of areas $\geq 8^\circ$ | Average (no. craters per 10 km^2) | % of areas ≥ 78 craters per 10 km^2 | Average (%) | % of areas $\geq 7\%$ | | | |
| 4 | 2.39 | 2.37 | 58 | 0.00 | 0.04 | 0.031 | 0.44 | 0.02 | 3 |
| 11 | 2.32 | 1.96 | 46 | 0.00 | 0.00 | 0.000 | 0.32 | 0.00 | 1 |
| 24 | 2.65 | 3.04 | 81 | 0.38 | 0.00 | 0.011 | 0.41 | 0.00 | 2 |

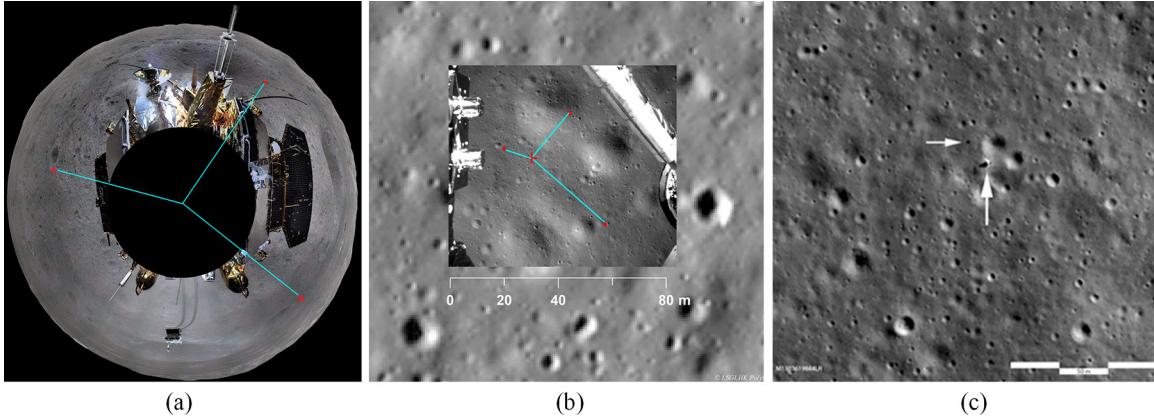


Figure 11. Localization of the Chang'E-4 lander. (a) Three small craters marked as red dots on the ground panorama image. (b) The corresponding positions of the craters marked on the descent image, which was geo-referenced with the LRO NAC image. The red cross indicates the lander location obtained by optimal cartographic triangulation. (c) The LRO NAC image (M1303619844LR) taken on 1 February 2019, showing the real locations of the lander and rover as indicated by the white arrows.

to an engineering constraint, but they worked fine as we were interested in the subregions of relatively favorable conditions.

We carried out the above analysis for all 25 subregions. The subregions (1–8) in the western part of the targeted landing region have relatively large slopes and rock abundances. Their crater densities are all below the threshold. The subregions (9–15) in the middle part have fewer slopes and rock abundances. Their crater densities are gradually increased. The subregions (16–25) in the eastern part have relatively large crater densities and slopes. Their rock abundances are moderate. For the occlusions to the Sun and the relay satellite, the first two subregions in the west and several subregions in the east (e.g., 19–23) have relatively large occlusions compared with other subregions. Comparing the subregions in the western, central, and eastern parts of the landing region, subregions 4, 11, and 24 show overall superiorities as compared with others in their neighborhoods. Therefore, they were short-listed for further consideration. The locations of the three short-listed subregions are shown in Figure 10b.

Table 1 lists the statistics of slopes, occlusions, crater densities, and rock abundances of the three short-listed subregions 4, 11, and 24. Their average slopes, crater densities, rock abundances, and occlusions to the Sun and relay satellite were further compared. From Table 1, it can be seen that subregion 11 shows the best performance in terms of all the aspects. Subregion 4 was ranked as the last, as it has a relatively high rock abundance and more serious occlusions to both the Sun and relay satellite. Subregion 11 was finally selected as the landing site with the highest priority, and Chang'E-4 actually landed in this subregion, with the exact location marked by a red cross in Figure 10b.

Landing Site Localization and Analysis

Localization of the Chang'E-4 Lander

On 3 January 2019, Chang'E-4 successfully landed in the Von Kármán crater. Identifying the exact location of the lander within the landing region and with respect to other surface features as soon as possible after landing was critical for planning science and engineering activities in the initial stages of surface exploration. The identification of other nearby features was also needed in traverse planning for the rover over the course of the mission. This was accomplished within two hours of landing before the rover drove off the lander. The related procedures involved Doppler positioning of the orbit track, reconstructing the entry, descent, and landing (EDL) process using returned descent images, and locating common features in the orbiter, descent, and ground images.

The navigation team determined the location of the lander at 45.5°S , 177.6°E , by Doppler positioning and orbit determination, which offered an initial location of the lander. A series of descent images collected by a descent camera mounted on the lander during the EDL process were used to reconstruct the lander's descent track, and the endpoint of the descent track was already close to the lander location. Finally, a ground panorama image, taken by the terrain camera mounted on top of the lander after landing, was used for the precise localization of the lander. As shown in Figure 11a, three meter-sized craters were manually identified on the ground panorama, and their centers were marked with red dots. Their corresponding positions on the descent image were then manually identified and marked with red dots as shown in Figure 11b. The descent image was geo-referenced to the LRO NAC image (M134022629L), as shown in the background in Figure 11b. The LRO NAC image was ortho-rectified using the Integrated Software for Imagers and Spectrometers software, which was already in the Mean Earth/Polar Axis reference system with planetocentric coordinates. The latitude and longitude coordinates of the lander were then calculated based on the optimal cartographic triangulation (Li *et al.* 2004) using these three

terrain features, which were in the same cartographic system of the used LRO NAC image. The elevation of the lander was measured from the DTM of the same location. The determined landing location of Chang'E-4 was at 45.4561°S, 177.5892°E, and at -5926 m elevation. The elevation was with respect to a reference sphere of radius 1737.4 km.

One week after the landing (on 11 January 2019), the LROC team at Arizona State University also identified the location of the Chang'E-4 lander at 45.457°S, 177.589°E, plus or minus 20 meters (<http://lroc.sese.asu.edu/posts/1087>), based on the co-registration of the Chang'E-4 descent frames and the NAC image (M1298916428LR). Liu *et al.* (2019) also located the Chang'E-4 landing site as 45.4446°S, 177.5991°E with an elevation of -5935 m using the digital orthophoto map and DTM of Chang'E-2 as geo-reference data, whose relative position to the surrounding terrain features is consistent with our results.

About one month later, after the successful landing of Chang'E-4, NASA's LRO passed by the Chang'E-4 landing region on 1 February 2019. The LRO NAC collected an image (M1303619844LR) of the landing region with a spatial resolution of 0.85 m/pixel, as shown in Figure 11c, on which the Chang'E-4 lander (the white dot with a dark shadow) and the Jade Rabbit-2 rover (the dark dot) can be clearly seen, as indicated by the white arrows. Comparing Figure 11b and 11c, it can be seen that the lander's location, as determined by our approach, is generally consistent with its real location, as imaged by the LRO NAC.

Analysis Around the Landing Site

After determining the lander's location, the analysis of its surrounding environment is vital for planning the subsequent science and engineering activities. We first examined the detailed terrain occlusions at the landing site. The approach described in the section "Occlusion Analysis" was adopted to analyze the occlusions at the landing site induced by the terrain, and the results are shown in Figure 12. Specifically, 360 geodesic lines were cast from the landing location at an azimuth interval of 1° as shown in Figure 12a. The position with the largest altitude angle induced by the nearby terrain was denoted by the endpoint of each geodesic line. Places with no geodesic lines visible are due to the terrain occlusions that happened in close ranges. Similarly, the relatively large occlusions were caused by the east-west rim of the Von Kármán crater. Overall, the terrain occlusion angles are generally less than 3° at the landing location. Figure 12b illustrates the relationships among the terrain occlusions, solar altitude angles, and altitude angles of the relay satellite at the landing location for the six-month period after landing, from 3 January to 3 July 2019. It can be seen that the solar altitude angles and the altitude angles of the relay satellite are both much higher than the terrain occlusion angles at the landing location, which indicates its excellent visibility to the Sun and relay satellite.

For a detailed analysis of surface slopes and geometric information of small surface features around the landing location, higher resolution DTMs are required. However, at the time when Chang'E-4 landed, no high-resolution stereo pair of LRO NAC images had been collected around the landing site. Therefore, generating high-resolution DTMs from stereo images using the traditional photogrammetric approach was not possible. We developed an innovative SFS method for generating pixel-wise lunar DTMs from a single image with the constraint of a lower-resolution DTM (Wu *et al.* 2018a). Given a single image with a known light source, the SFS method is able to refine a lower-resolution DTM covering the same image area to higher resolution, the same as the image resolution, by using shading information to optimize regularization with respect to shape reconstruction (Kirk *et al.* 2003). Details about this SFS method can be found in our previous publications (Wu *et al.* 2018a; Liu *et al.* 2018). The developed SFS method was applied to the

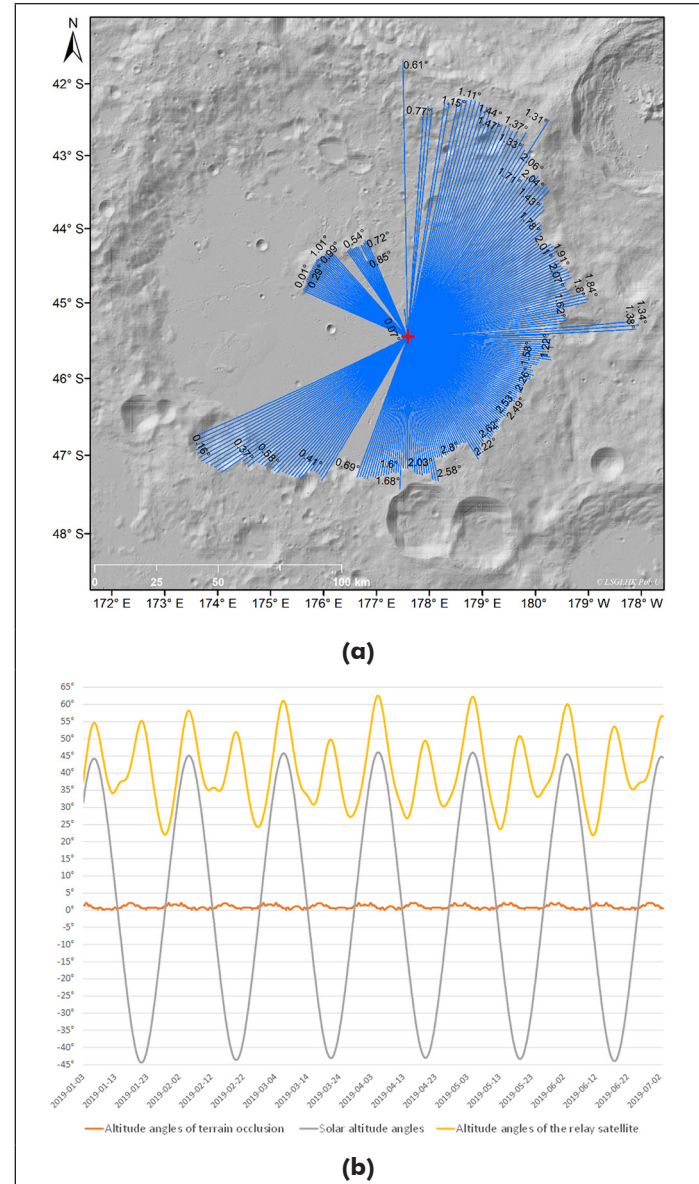


Figure 12. Occlusion analysis at the landing site. (a) The geodesic lines cast from the landing location (the red cross) at an interval of 1° and (b) the relationships among the terrain occlusions, solar altitude angles, and altitude angles of the relay satellite at the landing location for the six-month period after landing.

1.5 m/pixel LRO NAC image (M134022629L), and the SLDEM, with a resolution of 60 m used as the constraint, from which a high-resolution DTM (1.5 m/pixel) was generated, as shown in Figure 13. The differences in elevation between the SFS DTM and a photogrammetric DTM generated later using a stereo pair of NAC images is less than 5% (Liu and Wu 2020).

The upper row of Figure 13 shows a side-by-side comparison of the low-resolution SLDEM and the generated high-resolution SFS DTM, the latter showing overall consistent geometry with the former but providing much better details of the terrain features. The landing location of Chang'E-4 is marked in the SFS DTM and LRO NAC image with cyan crosses. It can be seen that the small craters around the landing location are clearly visible on the SFS DTM, but they are entirely missing on the SLDEM.

Based on the 1.5 m/pixel SFS DTM, a slope map with a baseline of 3 m was generated as shown in Figure 14a, from which it can be seen that the eastern part of the landing site has relatively larger slopes and the western part is relatively flat. For any point in the DTM, an aspect is calculated, which is the angle from the direction of the maximum slope at that point to the north direction. An aspect map was then generated to show the orientations of the slopes, as shown in Figure 14b. From the slope and aspect maps, the slope of the lander location is measured to be about 4.5° , and its aspect is toward southwest with an angle of 205° from the north.

The high-resolution DTM also enables the measurement of the detailed geometric information of small terrain features (e.g., diameters and depths of small craters) around the landing location. For instance, the three small craters surrounding the lander (see in Figure 13) have diameters of about 20–30 m and depths of about 2–2.6 m. These three craters all have a depth–diameter ratio of about 0.1. The shortest distance from the lander to any of these three craters is about 13 m. From the aforementioned rock abundance map, measurements show that the rock abundance around the landing location is almost 0. This type of detailed information is vital for the operation of instruments on the lander and for the surface operations of the rover.

Conclusions and Discussion

This paper presents the efforts concerning the landing site selection for the Chang'E-4 mission by jointly analyzing topographic and geomorphological features. Additionally, this paper describes the localization of the landing site and the analytical methods used to understand its surrounding area. The investigation leads to the following conclusions:

1. The DTM, with a resolution of 30 m generated from the integrated processing of Chang'E-2 images and LOLA data, reveals that the inner part of the Von Kármán crater is

quite flat. In the targeted landing region, about 5% of the areas have slopes larger than 8° . In addition, within the region there is satisfactory visibility to both the Sun and relay satellite, which are not occluded by the terrain surface in most areas.

2. The eastern part of the targeted landing region has relatively higher crater density. Overall, on average the crater density is about 60 craters (≥ 70 m in diameter) in a circular window of 10 km^2 . Most of the landing region is rock-free based on our investigation, and most of the rocks are located around large impact craters and on the slopes of hills.
3. The joint analysis of surface slopes, occlusions to the Sun and relay satellite, crater densities, and rock abundances identified three subregions inside the targeted landing region. The one located close to the center of the region was recommended as the site with the highest priority, and the Chang'E-4 eventually landed at this site.
4. The integrated processing of orbiter, descent, and ground images identified the precise location of the Chang'E-4 lander within two hours after its successful landing, positioning it at 45.4561°S , 177.5892°E , and at -5926 m in elevation. This location is consistent with the actual observed location of the Chang'E-4 lander as fixed by the LRO NAC image one month later.
5. Detailed occlusion analysis around the landing location reveals that the lander has excellent visibility to the Sun and relay satellite. A detailed slope analysis around the landing location using an SFS DTM with a high resolution of 1.5 m/pixel indicates that the lander is on a slope of about 4.5° toward the southwest. The rock abundance around the landing location is almost 0.

The analytical methods described in this paper have demonstrated their effectiveness in real operations of the Chang'E-4 mission. The developed methods and results can benefit future missions of soft landings on the Moon and other celestial bodies.

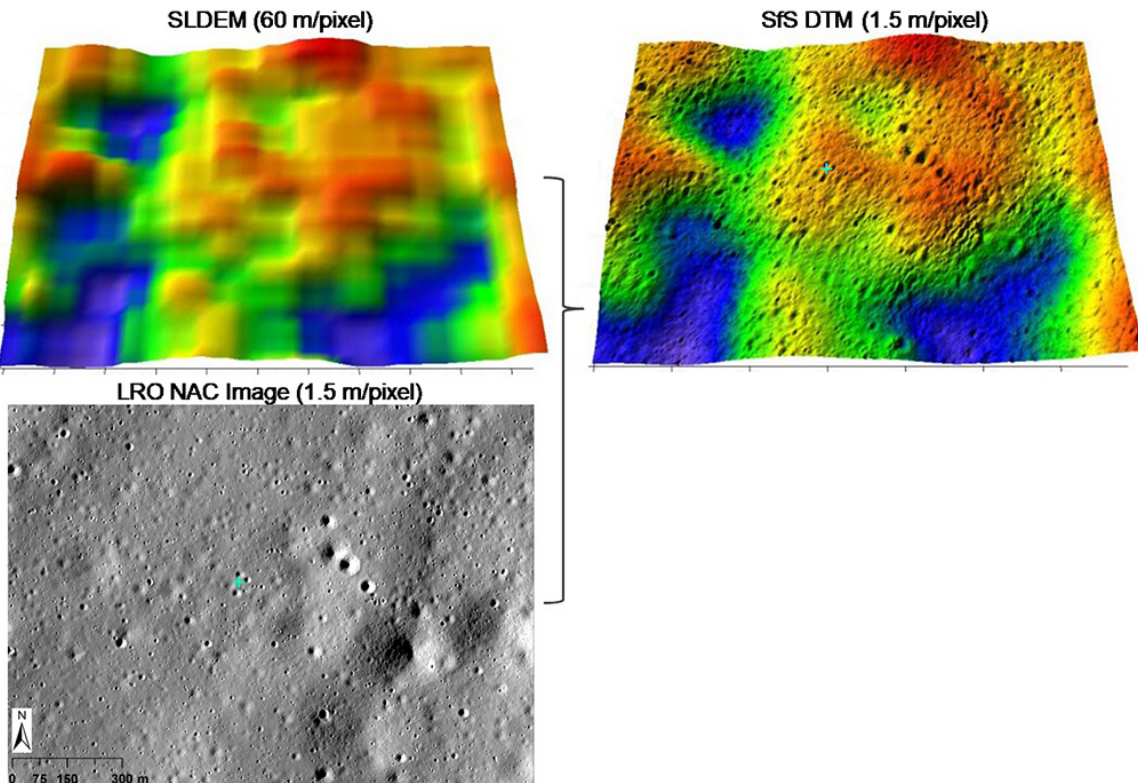


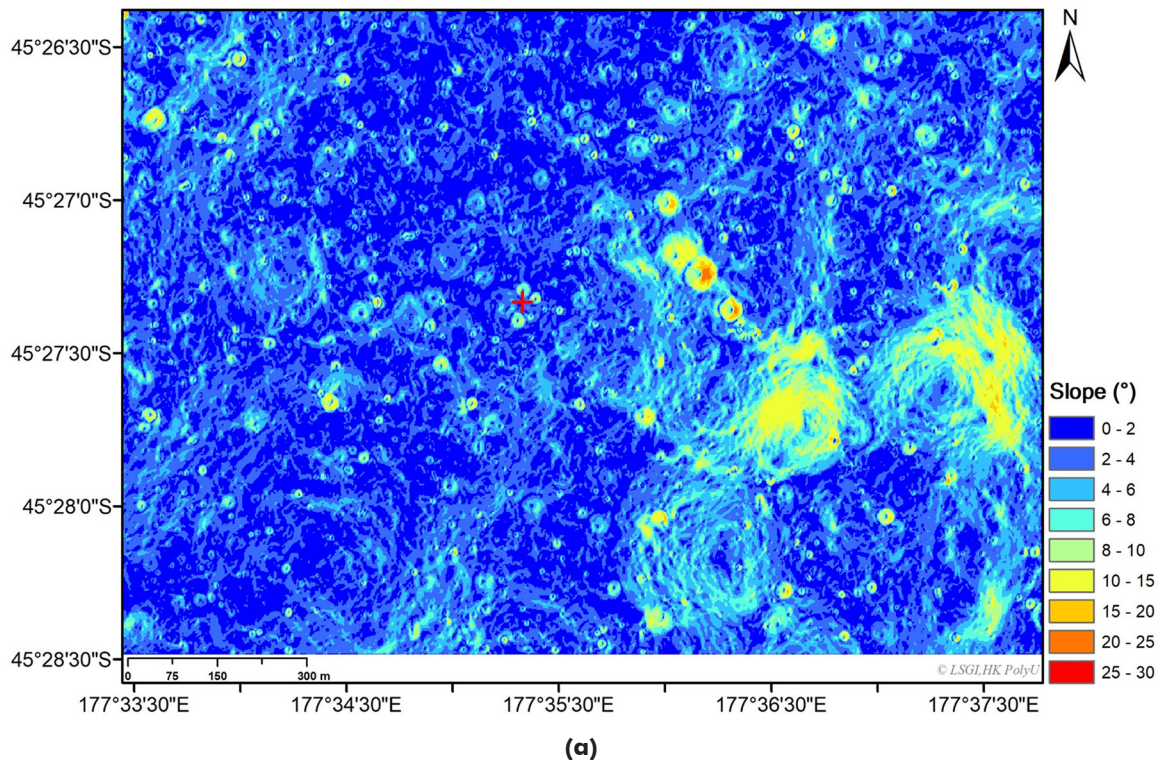
Figure 13. High-resolution DTM generated by the SFS method. The landing location is marked with a cyan cross. The elevations of the DTMs are exaggerated three times for better visualization.

Acknowledgments

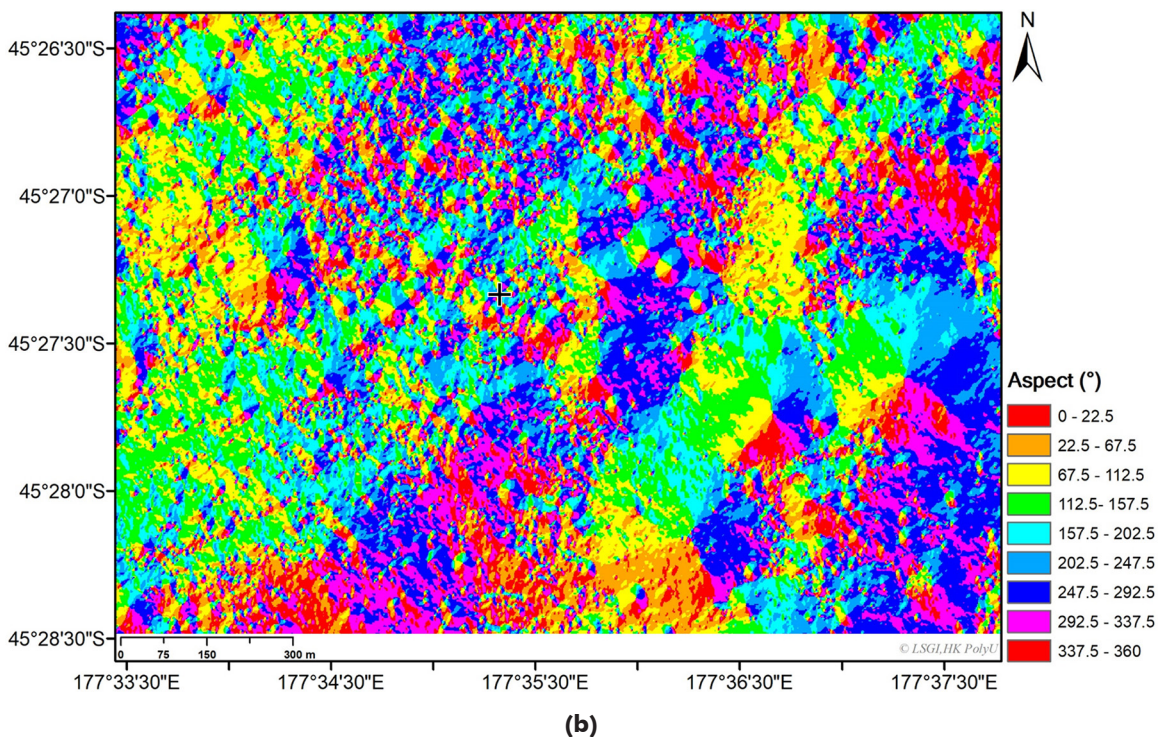
This work was funded by China Academy of Space Technology (Project No: 17CPIT/HK0102) and a grant from the Research Grants Council of Hong Kong (Research Impact Fund - Project No: R5043-19). The work was also supported by a grant from the National Natural Science Foundation of China (Project No: 41671426). The authors would like to thank everyone who worked on the archives of the imagery and datasets used in this research for making them publicly available.

References

- Bandfield, J. L., R. R. Ghent, A. R. Vasavada, D. A. Paige, S. J. Lawrence and M. S. Robinson. 2011. Lunar surface rock abundance and regolith fines temperatures derived from LRO Diviner Radiometer data. *Journal of Geophysical Research: Planets* 116(E12).
- Barker, M. K., E. Mazarico, G. A. Neumann, M. T. Zuber, J. Haruyama and D. E. Smith. 2016. A new lunar digital elevation model from the Lunar Orbiter Laser Altimeter and SELENE Terrain Camera. *Icarus* 273:346–355.



(a)



(b)

Figure 14. Detailed slope analysis around the landing site. (a) The slope map calculated with a baseline of 3 m and (b) the corresponding aspect map. The lander's location is marked on the maps with red and black crosses, respectively.

- Brady, T., E. Robertson, C. Epp, S. Paschall and D. Zimpfer. 2009. Hazard detection methods for lunar landing. Pages 1–8 in *Proceedings of the 2009 IEEE Aerospace Conference*.
- De Rosa, D., B. Bussey, J. T. Cahill, T. Lutz, I. A. Crawford, T. Hackwill, S. van Gasselt, G. Neukum, L. Witte and A. McGovern. 2012. Characterization of potential landing sites for the European Space Agency's Lunar Lander project. *Planetary and Space Science* 74 (1):224–246.
- Di, K., M. Zhu, Z. Yue, Y. Lin, W. Wan, Z. Liu, S. Gou, B. Liu, M. Peng, Y. Wang, S. Niu, J. Zhang, J. Li, J. Xie, L. Xi, J. Yang and B. Xue. 2019. Topographic evolution of Von Kármán crater revealed by the lunar rover Yutu-2. *Geophysical Research Letters* 46 (22):12764–12770.
- Golombek, M. and D. Rapp. 1997. Size frequency distributions of rocks on Mars and Earth analog sites: Implications for future landed missions. *Journal of Geophysical Research: Planets* 102 (E2):4117–4129.
- Golombek, M. P., A. Haldemann, N. Forsberg-Taylor, E. N. Di Maggio, R. D. Schroeder, B. M. Jakosky, M. Mellon and J. Matijevic. 2003. Rock size-frequency distributions on Mars and implications for Mars Exploration Rover landing safety and operations. *Journal of Geophysical Research* 108 (E12):8086.
- Golombek, M., D. Kipp, N. Warner, I. J. Daubar, R. Fergason, R. L. Kirk and B. A. Campbell. 2017. Selection of the InSight landing site. *Space Science Reviews* 211 (1–4):5–95.
- Hu, H. and B. Wu. 2019. Planetary3D: A photogrammetric tool for 3D topographic mapping of planetary bodies. *ISPRS Annals of the Photogrammetry, Remote Sensing and Spatial Information Sciences* IV-2/W5:519–526.
- Hu, H., C. Chen, B. Wu, X. Yang, Q. Zhu and Y. Ding. 2016. Texture-aware dense image matching using ternary census transform. *ISPRS Annals of the Photogrammetry, Remote Sensing and Spatial Information Sciences* III-3:59–66.
- Huang, J., Z. Xiao, J. Flahaut, M. Martinot, J. Head, X. Xiao, M. Xie and L. Xiao. 2018. Geological characteristics of Von Kármán crater, northwestern south Pole Aitken basin: Chang'E 4 landing site region. *Journal of Geophysical Research: Planets* (123):1684–1700.
- Jia, Y., Y. Zou, J. Ping, C. Xue, J. Yan and Y. Ning. 2018. The scientific objectives and payloads of Chang'E-4 mission. *Planetary and Space Science* 162:207–215.
- Karney, C. F. 2013. Algorithms for geodesics. *Journal of Geodesy* 87 (1):43–55.
- Kirk, R. L., E. Howington-Kraus, B. Redding, D. Galuszka, T. M. Hare, B. A. Archinal, L. A. Soderblom and J. M. Barrett. 2003. High-resolution topomapping of candidate MER landing sites with Mars Orbiter Camera narrow-angle images. *Journal of Geophysical Research: Planets* 108 (E12):8088.
- Li, C., D. Liu, B. Lu, X. Ren, J. Liu, Z. He, W. Zuo, X. Zeng, R. Xu, X. Tan, X. Zhang, W. Chen, R. Shu, W. Wen, Y. Su, H. Zhang and Z. Ouyang. 2019. Chang'E-4 initial spectroscopic identification of lunar far-side mantle-derived materials. *Nature* 569:378–382.
- Li, F., H. Zhang, X. Wu, J. Ma and L. Lu. 2017. Influence analysis of terrain of the far side of the Moon on soft-landing. *Journal of Deep Space Exploration* 4 (2):143–149.
- Li, R., K. Di, L. H. Matthies, W. M. Folkner, R. E. Arvidson and B. A. Archinal. 2004. Rover localization and landing-site mapping technology for the 2003 Mars exploration rover mission. *Photogrammetric Engineering and Remote Sensing* 70 (1):77–90.
- Li, Y. and B. Wu. 2018. Analysis of rock abundance on lunar surface from orbital and descent images using automatic rock detection. *Journal of Geophysical Research: Planets* 123 (5):1061–1088.
- Liu, W. C., B. Wu and C. Wöhler. 2018. Effects of illumination differences on photometric stereo shape-and-albedo-from-shading for precision lunar surface reconstruction. *ISPRS Journal of Photogrammetry and Remote Sensing* 136:58–72.
- Liu, W. C. and B. Wu. 2020. An integrated photogrammetric and photoclinometric approach for illumination-invariant pixel-resolution 3D mapping of the lunar surface. *ISPRS Journal of Photogrammetry and Remote Sensing* 159:153–168.
- Liu, J., X. Ren, W. Yan, C. Li, H. Zhang, Y. Jia, X. Zeng, W. Chen, X. Gao, D. Liu, X. Tan, X. Zhang, T. Ni, H. Zhang, W. Zuo, Y. Su and W. Wen. 2019. Descent trajectory reconstruction and landing site positioning of Chang'E-4 on the lunar farside. *Nature Communications* 10:4229.
- Pajola, M., S. Rossato, E. Baratti, R. Pozzobon, C. Quantin, J. Carter and P. Thollot. 2017. Boulder abundances and size-frequency distributions on Oxia Planum-Mars: Scientific implications for the 2020 ESA ExoMars rover. *Icarus* 296:73–90.
- Wang, Y. and B. Wu. 2017. Improved large-scale slope analysis on Mars based on correlation of slopes derived with different baselines. *International Archives of the Photogrammetry, Remote Sensing and Spatial Information Sciences* 42.
- Wang, Y. and B. Wu. 2019. Active machine learning approach for crater detection from planetary imagery and digital elevation models. *IEEE Transactions on Geoscience and Remote Sensing* 57 (8):5777–5789.
- Wilhelms, D. E., F. John and N. J. Trask. 1987. *The Geologic History of the Moon*. Washington, D.C.: U.S. Geological Survey.
- Wu, B., F. Li, L. Ye, S. Qiao, J. Huang, X. Wu and H. Zhang. 2014a. Topographic modeling and analysis of the landing site of Chang'E-3 on the Moon. *Earth and Planetary Science Letters* 405:257–273.
- Wu, B., H. Hu and J. Guo. 2014b. Integration of Chang'E-2 imagery and LRO laser altimeter data with a combined block adjustment for precision lunar topographic modeling. *Earth and Planetary Science Letters* 391:1–15.
- Wu, B., W. C. Liu, A. Grumpe and C. Wöhler. 2018a. Construction of pixel-level resolution DEMs from monocular images by shape and albedo from shading constrained with low-resolution DEM. *ISPRS Journal of Photogrammetry and Remote Sensing* 140:3–19.
- Wu, B., J. Huang, Y. Li, Y. Wang and J. Peng. 2018b. Rock abundance and crater density in the candidate Chang'E-5 landing region on the Moon. *Journal of Geophysical Research—Planets* 123 (12):3256–3272.
- Wu, W. R., Q. Wang, Y. H. Tang, J. Z. Liu and L. L. Lu. 2017. Design of Chang'E-4 lunar farside soft-landing mission. *Journal of Deep Space Exploration* 4 (2):111–117.